Available online at www.sciencedirect.com

ScienceDirect

Advances in Space Research 72 (2023) 4420–4434

ADVANCES IN SPACE RESEARCH (a COSPAR publication)

www.elsevier.com/locate/asr

Applying support vector machine (SVM) using GPS-TEC and Space Weather parameters to distinguish ionospheric disturbances possibly related to earthquakes

Angela Melgarejo-Morales [a,*], G. Esteban Vazquez-Becerra [b], J.R. Millan-Almaraz [c], Carlos A. Martinez-Felix [c], Munawar Shah [d,e]

[a] *SCiESMEX, LANCE, Instituto de Geofisica, Unidad Michoacan, Universidad Nacional Autonoma de Mexico, Morelia C.P. 58089, Michoacan, Mexico*
[b] *Department of Earth and Space Science, Autonomous University of Sinaloa, Culiacan C.P. 80040, Sinaloa, Mexico*
[c] *Department of Physics-Mathematics Science, Autonomous University of Sinaloa, Culiacan C.P. 80040, Sinaloa, Mexico*
[d] *Department of Space Science, Space Education and GNSS Lab, National Center of GIS and Space Application, Institute of Space Technology, Islamabad, Pakistan*
[e] *College of Surveying and GeoInformatics, Tongji University, Shanghai, C.P. 200092, China*

Received 5 September 2022; received in revised form 12 August 2023; accepted 16 August 2023
Available online 22 August 2023

Abstract

The effort to identify and comprehend potential earthquake-related phenomena shares a common goal: successful earthquake forecasting. Advancements in science and technology have made this goal multidisciplinary. Currently, possibly earthquake-related anomalies in the Vertical Total Electron Content (VTEC) of the Earth's ionosphere are being investigated. Global Navigation Satellite Systems (GNSS) can be used to calculate this ionospheric parameter. In this research work, GPS VTEC was calculated for periods between the years 2015 and 2019. The selection of this periods considered both seismically active and non-seismically areas in Mexico. The $M_w \geq 5$ earthquakes under study were registered by the National Seismological Service. Moreover, different geomagnetic storm and solar activity parameters, such as the geomagnetic equatorial Dst index and the F10.7 index, were analyzed. Additionally, the daily average and monthly mean number of sunspots (R, SSN, respectively) were included as a direct, long-term record of the development of the solar cycle. To the periods under study different statistical methods were applied, such as Mean-Square Error (MSE) and cross-correlation. The above aims to apply a machine learning technique capable of classifying between periods with seismic and non-seismic activity. The features were constructed using statistical data and results from the implemented analysis. Furthermore, Principal Component Analysis (PCA) was applied to reduce the feature vector dimensions, and accuracy scores were compute using k-fold cross-validation. The results from the Support Vector Machine (SVM) model indicated an accuracy of 88.9% for the training set, and an accuracy of 80% was obtained for the test set. One of the limitations of the current study was the sample size. However, the present initial approach for classifying seismic events from non-seismic periods using SVM demonstrated promising results when considering the indicated parameters and the days under study.

Keywords: Earthquakes; GPS-TEC; Geomagnetic and solar indices; Support Vector Machine; Statistics

---

1. Introduction

Controversy over the extent to which seismic precursors are considered a suitable factor in earthquake forecasting is

---

* Corresponding author.
E-mail addresses: angela@igeofisica.unam.mx (A. Melgarejo-Morales), gvazquez@uas.edu.mx (G. Esteban Vazquez-Becerra), jrmillan@uas.edu.mx (J.R. Millan-Almaraz), carlosmartinez@uas.edu.mx (C.A. Martinez-Felix), munawar.shah@mail.ist.edu.pk (M. Shah).

https://doi.org/10.1016/j.asr.2023.08.028

comprehensible, given that earthquakes are random and highly non-linear natural phenomena. Over the past five hundred years, more than seven million people have lost their lives due to earthquakes and many others have witnessed the destruction of their food sources and economies (Bolt, 1993). In the case of Mexico, its geology reflects that large part of its territory is subject to enormous stress, resulting in earthquakes (Bolt, 2001). Mexico is particularly susceptible to the complex interactions between the North American, Pacific, Cocos, Caribbean, and Rivera tectonic plates, making the Pacific coast regions of Mexico a focal point of interest for this study.

Currently, GPS-TEC provides insights into the seismic preparation zone in the Earth's ionosphere using radio signals. Extensive research on ionospheric perturbations likely associated with earthquakes has been published, and it has emerged as a reliable parameter to consider in the field of earthquake forecasting (Ouzounov et al., 2011; Tsai et al., 2018; Barkat et al., 2018; Shah et al., 2021; Shah et al., 2022, and references therein). For example, Sotomayor-Beltran (2019) detected a negative perturbation in the Vertical Total Electron Content (VTEC) ten days prior to the Pedernales earthquake in Ecuador ($M_w = 7.8$). The study used Global Ionospheric Maps (GIMs) from the Center for Orbit Determination in Europe (CODE) to extract the ionospheric parameter, with reported solar and geomagnetic activity levels characterized as quiet. Similarly, Melgarejo-Morales et al. (2020) analyzed VTEC data derived from GPS during earthquakes of Mw $\geq$ 5.1, revealing that the majority of the studied earthquakes were preceded by periods of non-quiet geomagnetic activity. Astafyeva and Heki (2011) investigated VTEC variations during a period of solar and geomagnetic quietude, highlighting the challenges in identifying earthquake precursors due to the alterations induced by Space Weather. Furthermore, Shah et al. (2019) detected atmospheric anomalies before and after various earthquakes ($M_w > 6$). Under the Lithosphere–Atmosphere–Ionosphere Coupling (LAIC) hypothesis, the authors identified perturbations within one month preceding all the analyzed seismic events. Additionally, previous studies have reported TEC perturbations prior to large earthquakes (Karatay et al., 2010; Le et al., 2011; Arikan et al., 2016; Shah et al., 2020; Shah et al., 2022).

On the other hand, research has produced conflicting evidence regarding the role of solar activity and geomagnetic field disturbances in triggering earthquakes (Love, 2013; Marchitelli et al., 2020; Akhoondzadeh and De Santis, 2022). The debate surrounding extraterrestrial factors in seismicity remains controversial. Odintsov et al. (2006), for example, suggested that the Sun, as the strongest energy source near the Earth, may potentially have a connection with different elements of solar activity and terrestrial processes.

Despite the lack of complete understanding regarding the physical mechanisms underlying these connections, several hypotheses have been proposed. These include the penetration of electric current vortices and magnetic field variations from the ionosphere into the electrically conductive lithosphere, resulting in additional mechanical forces within seismic rupture zones (Urata et al., 2018). Another hypothesis involves the deposition of solar wind energy into the polar ionosphere, leading to disturbances in air mass transfer and affecting the pressure balance on tectonic plates (Gousheva et al., 2003). Additionaly, the induction of eddy electric currents in faults has been postulated (Han et al., 2004). Although these studies revealed some important aspects on ionospheric perturbations preceding earthquakes, all the details are yet to be fully observed (Tsugawa et al. 2011). However, as mentioned by Delorey et al. (2017), continued advancements in technology, particularly in terms of instrumentation and techniques, are likely to unveil precursors for most of the earthquakes.

The aim of this research is to present a first approach to apply a machine learning technique for classifying between periods of seismic and non-seismic activity based on proposed features. Furthermore, the study aims to demonstrate significant differences between data recorded during seismic and non-seismic periods. The structure of this paper is organized as follows: Section II provides a description of the Materials and Methods utilized, Section III encompasses the Results and Discussions, and finally, the Conclusions are summarized in Section IV.

2. Materials and methods

Mexico exhibits different tectonic configurations across its territory. The regions along the Pacific coast, part of the Pacific Ring of Fire, are prone to register telluric activity. Thus, highly seismic regions. In fact, some of the largest earthquakes ever documented in Mexican history have occurred offshore the Jalisco region, such as those recorded in 1932 ($M_s = 8.1$) and 1995 ($M_w = 8$) (Singh et al., 1985; Courboulex et al., 1997). Despite the prevalence of seismic activity, certain regions in Mexico exhibit null or scarce seismic activity. These areas include Yucatan, Quintana Roo, Tamaulipas, Nuevo Leon, Coahuila, Campeche, and Chihuahua (Godinez-Dominguez et al., 2021).

2.1. Earthquake data

According to different studies, significant changes in the ionosphere have been observed before and after earthquakes of $M_w \geq 5.0$ (Singh et al. 2009; Muhammad et al., 2023). For this study, a total of 30 earthquakes of $M_w \geq 5.0$ occurred in Mexico between the years 2015 and 2019 were selected (Table 1). Additionally, a set of 20 non-seismic periods were selected (Table 2). The data for the non-seismic periods was collected from GPS stations located in the states of Quintana Roo and Chihuahua (Fig. 1). The selection of non-seismic periods prioritized time intervals that did not coincide with earthquakes registered in nearby seismic areas. According to

Table 1
The selected seismic events ($M_w \geq 5$) recorded in Mexico between 2015 and 2019, according to the National Seismological Service catalog (http://www.ssn.unam.mx/). The time, depth, magnitude and location of the earthquake is provided. "BCS" refers to Baja California Sur.

Event	Day	Month	Year	Time (UTC)	Depth (Km)	Magnitude (M_w)	Latitude N (°)	Longitude W (°)	Distance from station to the epicenter (Km)	State
1	22	04	2019	20:15:23	7	5.5	16	−98.55	158.80	Oaxaca
2	21	01	2019	11:57:19	35	5.8	15.42	−94.94	233.72	Oaxaca
3	19	01	2018	16:17:45	16	6.3	26.66	−111.10	749.07	BCS
4	03	11	2017	11:52:06	16.2	5.6	18.71	−106.51	406.10	Jalisco
5	24	09	2017	10:06:08	15.8	5.8	15.08	−94.33	214.98	Chiapas
6	23	09	2017	14:31:47	10	5	16.45	−94.99	163.07	Oaxaca
7	23	09	2017	12:53:04	22	6.1	16.49	−95.14	216.97	Oaxaca
8	23	09	2017	10:38:05	35	5.8	15.25	−94.58	209.71	Oaxaca
9	19	09	2017	07:53:10	11.7	5.6	14.79	−94.42	222.54	Chiapas
10	18	09	2017	14:19:14	15	5.8	15.25	−94.76	211.55	Oaxaca
11	12	09	2017	05:08:45	24.6	5.5	14.98	−94.01	179.50	Chiapas
12	11	09	2017	21:09:13	16.1	5.6	14.97	−94.05	183.66	Chiapas
13	10	09	2017	03:07:21	19.7	5.8	15.23	−94.63	205.00	Oaxaca
14	09	09	2017	04:54:49	23.4	5.6	14.74	−94.07	185.05	Chiapas
15	08	09	2017	04:49:17	45.9	8.2	14.76	−94.10	188.20	Chiapas
16	14	06	2017	07:29:04	107.1	6.9	14.72	−92.31	9.88	Chiapas
17	10	06	2017	18:47:30	9.8	5.5	13.98	−93.25	133.07	Chiapas
18	31	03	2017	09:58:05	101.5	5.3	15.59	−93.17	132.54	Chiapas
19	07	11	2016	03:50:19	94.9	5	15.87	−93.96	199.78	Chiapas
20	30	07	2016	13:53:13	14.2	5	13.98	−91.73	252.90	Chiapas
21	23	07	2016	08:51:51	20	5.4	14.46	−103.75	633.51	Michoacan
22	18	07	2016	19:02:15	71.9	5	14.56	−92.59	191.96	Chiapas
23	15	06	2016	13:46:54	71.3	5.3	13.98	−91.80	108.09	Chiapas
24	02	06	2016	02:23:07	6.2	5.6	18.13	−105.69	382.60	Jalisco
25	23	05	2016	19:20:39	130.1	5.3	16.64	−94.04	273.23	Chiapas
26	27	04	2016	12:51:18	20	6	14.29	−93.38	125.30	Chiapas
27	25	04	2016	07:07:12	10.4	6	14.53	−93.21	97.377	Chiapas
28	15	04	2016	14:11:24	12	6.1	13.25	−92.45	172.27	Chiapas
29	22	02	2015	14:23:13	16	6.2	18.64	−106.95	286.45	Jalisco
30	12	02	2015	15:50:56	15	5.5	19.16	−105.91	179.79	Jalisco

Table 2
Non-seismic periods selected between 2018 and 2015.

Period	Days	Month	Year	State
1	01–14	02	2018	Quintana Roo
2	21–06	02 – 03	2018	Quintana Roo
3	01–14	03	2018	Quintana Roo
4	18–31	03	2018	Quintana Roo
5	16–29	04	2018	Quintana Roo
6	11–24	05	2018	Quintana Roo
7	01–14	01	2017	Quintana Roo
8	11–24	01	2017	Quintana Roo
9	19–01	01 – 02	2017	Chihuahua
10	14–27	02	2017	Quintana Roo
11	02–15	03	2017	Chihuahua
12	18–31	07	2017	Quintana Roo
13	01–14	12	2017	Chihuahua
14	13–26	12	2017	Quintana Roo
15	05–18	09	2016	Quintana Roo
16	16–29	09	2016	Chihuahua
17	07–20	11	2016	Chihuahua
18	16–29	11	2016	Quintana Roo
19	01–14	12	2016	Chihuahua
20	23–06	11 – 12	2015	Quintana Roo

the catalog of the National Seismological Service, no earthquakes with $M_w \geq 5.0$ were recorded during the non-seismic periods.

Each period consisted of 14 days. For the earthquake periods, 8 days before the main shock, the earthquake day and 5 days after. The geographical distribution of the selected earthquakes and the GPS stations are shown in Fig. 1. Almost half of the earthquakes studied were recorded in Chiapas (17 events), followed by Oaxaca (7 events), Jalisco (4 events) and Michoacan and Baja California Sur (1 event each), which are highlighted in Fig. 1.

2.2. GPS satellite data

The selection of events and stations in the study area was based on data availability. Specifically, the GPS networks that operate with high performance and reliability were the objective. After evaluating the availability, sampling frequency, and data quality; spatial data with a frequency of 1 Hz were downloaded from 11 GPS stations. These selected stations are represented as blue circles in Fig. 1, and their geographic locations are listed as a Table S3 in the Supplementary Material.

In Fig. 1, it can be seen that most of the earthquakes were concentrated in the Southeast part of Mexico (approximately 25 out of 30 events, 83% of the total). Also, most of the earthquakes considered in this study occurred in 2017 (15 out of 30 earthquakes, 50%). Meanwhile, the non-seismic events mostly correspond to periods in the year 2017 (40% of the total, Table 2). On the other hand, the largest magnitude recorded in the dataset was $M_w = 8.2$, followed by $M_w = 6.9$. Additionally, 12 earthquakes had a magnitude $5 \leq M_w \leq 5.5$, while 18 earthquakes had a magnitude $M_w > 5.5$.

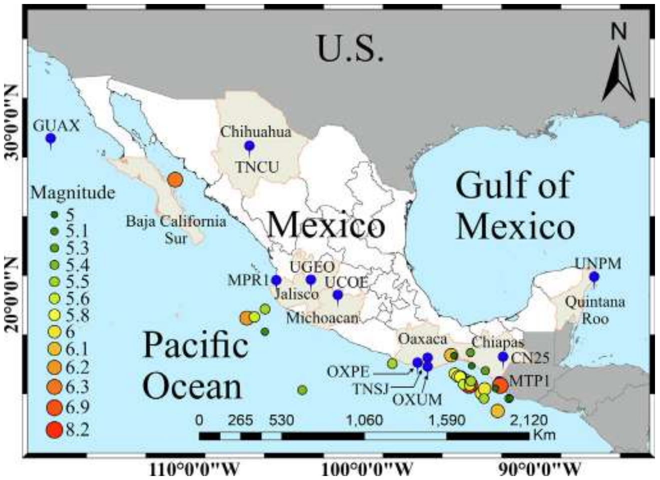

Fig. 1. Location of the $M_w \geq 5.0$ earthquakes that occurred in Mexico between 2015 and 2019, as reported by the National Seismological Service. Different dot colors and sizes are used to represent the magnitude. The selected GPS stations are denoted with blue dots.

2.3. Data processing

The GPS satellites broadcast important information about the atmospheric layers. Specifically, the system dual-frequency capability enables measuring the phase difference between two signals of different frequencies transmitted by each satellite (L1 = 1575.42 MHz and L2 = 1227.60 MHz). This process enables the calculation of the ionospheric parameter known as Total Electron Content (TEC). As described by Sardon et al. (1993), TEC represents the total number of free electrons present in the ionosphere along the line of sight between the satellite's altitude and a ground-based receiver. The unit of measurement for TEC is TECU (Total Electron Content Units), where 1 TECU is equivalent to $10^{16} e/m^2$.

The software "RINEX_HO" (Marques et al. 2011) was used to calculate the ionospheric VTEC using pseudorange (PR_{Li}) measurements, as represented by Eq. (1).

$$\mathrm{TEC} = \frac{f_{L1}^2 f_{L2}^2}{40.3(f_{L2}^2 - f_{L1}^2)}\left[PR_{L1} - PR_{L2} - c(DCB_r + DCB_s) + \epsilon L1L2\right] \tag{1}$$

where $f_{Li} = (i = 1, 2)$ represents the GPS frequencies, DCB_r and DCB_s (in second units) are the polarization of the receiver and satellite differential code, respectively. That is, the hardware delays between the two frequencies. The speed of light in vacuum is denoted as c, and $\epsilon L1L2$ represents the non-modeled residual effects. This tool requires a RINEX observation file as input and utilizes the pseudorange measurements smoothed by the phase. The algorithm utilized for pseudorange smoothing follows the equations described by Teunissen (1991) and Jin (1996), with more detailed information provided in Marques et al. (2011).

Since solar activity is the primary driver of ionization in the ionosphere, it is important to consider various solar indices. This helps in identifying and discarding large-scale transient ionospheric disturbances that may arise due to Space Weather. Therefore, distinct geomagnetic and solar indices were consulted for both seismic and non-seismic periods. To study the long-term evolution of the solar cycle, the relative number of sunspots (R) and its monthly averaged data (SSN) were obtained from the Global Data Center SILSO in Brussels (https://wwwbis.sidc.be/silso/).

Additionally, due to its widely use as an indicator of solar activity the F10.7 index was consulted (https://www.spaceweather.gc.ca/). To further assess solar activity, the occurrence of large X-ray class (>M1) and very large X-ray class (>X1) solar flares was considered. Information about these solar flares was obtained from the catalogue available at https://www.wdcb.ru/stp/data. As indicators of geomagnetic activity, the Kp and Dst indices were consulted. The Kp index provides information about disturbances in the Earth's magnetic field, while the Dst index records variations in the equatorial ring current (Mayaud, 1980). Data for both indices were obtained from the NASA OMNIWeb data explorer (https://omniweb.gsfc.nasa.gov/form/dx1.html).

The solar energy indices mentioned above are presented in Fig. 2, providing an overview of the solar activity during the study periods. In general, these indices are used in the literature to distinguish between earthquake and Space Weather effects (Fig. 3).

The median $(\bar{x})$, standard deviation (σ), variance (σ^2), and the Mean Square Error (MSE) of the VTEC values were calculated. Also, the cross-correlation method was applied, the formula is provided in Eq. (2).

$$R_{xy}(m) = E\{x_{n+m} + y_n^*\} = E\{x_n y_{n-m}^*\}, -\infty < n < \infty \tag{2}$$

Where complex conjugation is denoted by the * symbol and E is the expected value operator. The cross-correlation method enable to identify a potential relation between two signals. In this particular case, the signals under study were the geomagnetic and solar indices for the entire periods.

From the cross-correlation results the following characteristics were evaluated: (1) the fit, this represents the amount of data at a given point, (2) symmetry, this indicates the degree of symmetry in the data, (3) kurtosis, this measures the relative shape of the data compared to a standard bell curve (for example, unimodal or bimodal) and can be interpreted as an attribute of the ridge, (4) inclination, this describes the deviation from horizontal symmetry in the data, and (5) skew, this evaluates the level of symmetry in the data.

Currently, the underlying physical processes of earthquakes are not fully understood. As a result, machine learning has emerged as a valuable tool for applying mathematical and statistical methods to earthquake forecasting. Machine learning involves the use of data to build models, with the primary objective being to classify data into specific classes. In this study, the supervised learning model Support Vector Machine (SVM) was implemented due to its high generalization capacity and

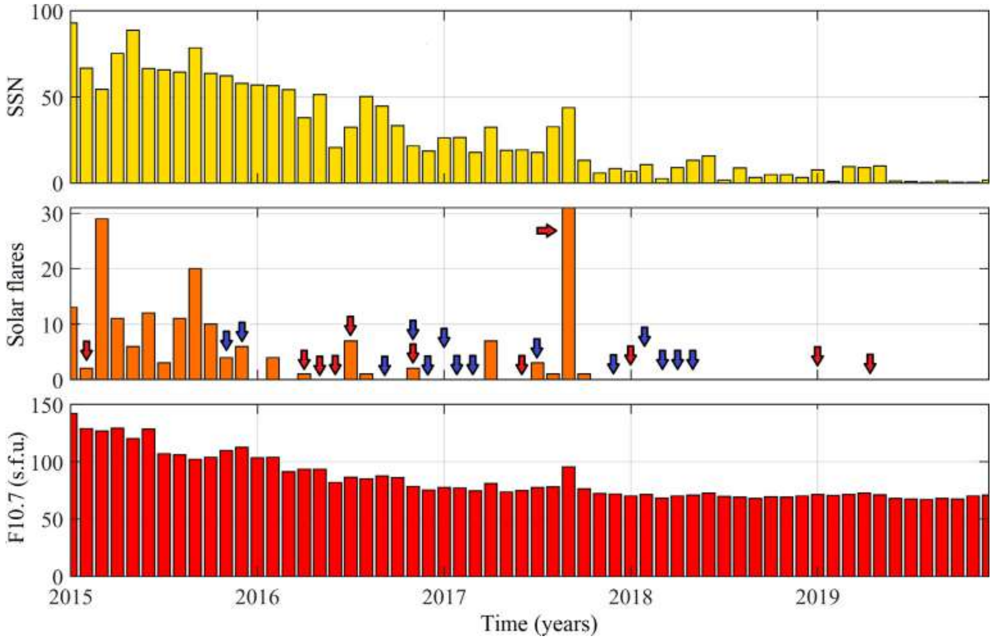

Fig. 2. Time series of solar activity indices for the period under study: monthly averaged values of Sunspot Number (SSN), number of solar flares of M1-X7 classes, and the F10.7 index. For solar flares, the month corresponding to a period under study is indicated with a colored arrow. The red arrow indicate seismic events and the blue arrow indicate non-seismic periods.

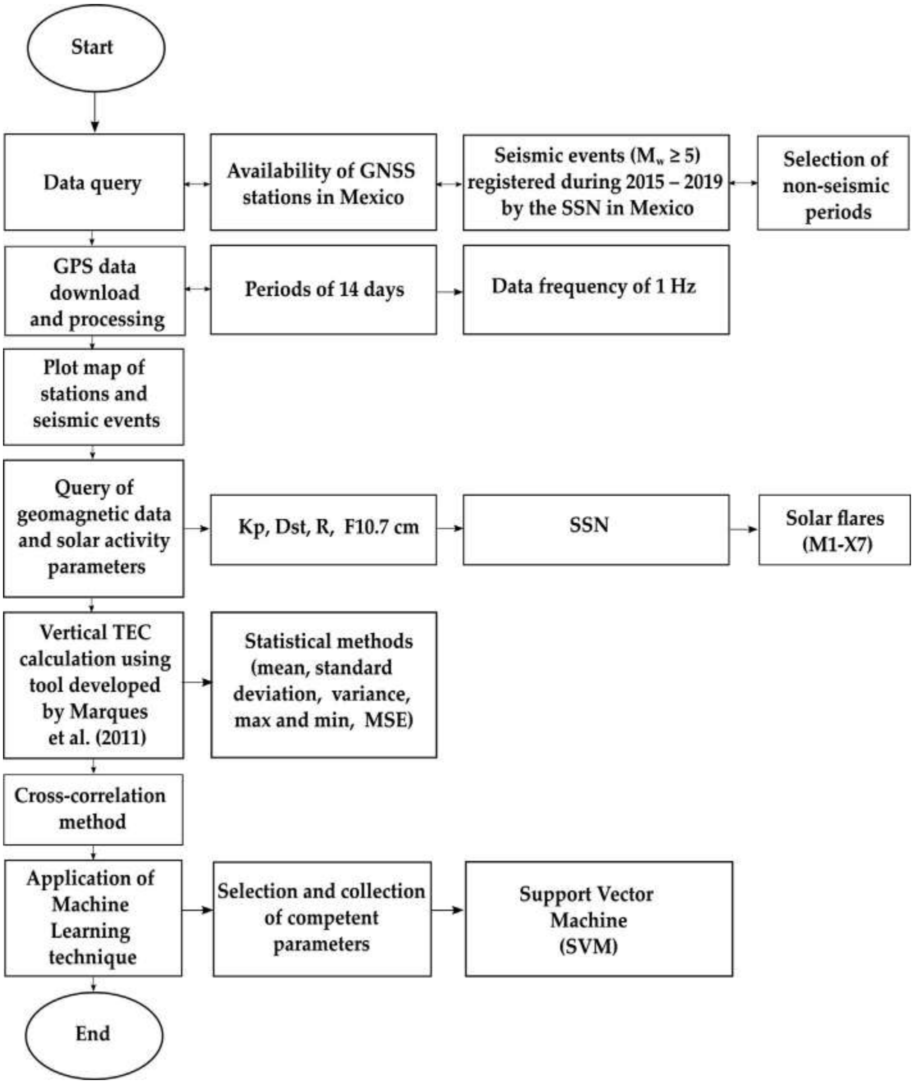

Fig. 3. Flow chart describing the applied methodology.

ability to handle real-world problems involving small sample sizes and nonlinear data, in addition to a strict theoretical base (Jiang et al., 2009).

Previous studies have reported significant TEC disturbances in the ionosphere up to nine days before an earthquake (Karatay et al., 2010; Deviren et al., 2014; Arikan et al., 2016). Moreover, Le et al. (2011) demonstrated that TEC disturbances are concentrated mainly from one to nine days before strong earthquakes, pointing out that these disturbances are more likely to be seen before an earthquake than on seismically inactive days. This is particularly relevant for the period examined in this study, which focuses on the eight days preceding an earthquake. Based on the aforementioned studies, the probability of detecting differences between seismic and non-seismic periods is favorable.

In general, an SVM can be described as follows: Given N vectors $\{x_1, x_2, ..x_n\}$, where each vector x_j consists of m characteristics $\{a_{j1}, a_{j2}\ , ..a_{jm}\}$ and belongs to one or two classes, C_1 or C_2. Therefore, if a hyperplane is discovered in the feature space that separates instances belonging to classes C_1 and C_2, it indicates that the provided data is linearly separable. Consequently, the primary objective of an SVM is to determine a hyperplane that effectively classifies all training vectors into their respective classes. Specifically, an SVM represents a linear discriminant function, denoted by:

$$S(x) = w^T x + b \tag{3}$$

Where x represents a feature vector, w denotes an m-dimensional weighting vector, and the scalar b represents the bias. The weight vector is orthogonal to the hyperplane and determines its direction, while the skew controls its position. In this sense, if a feature vector $\tilde{x}$ is given, then $S\left(\tilde{x}\right) = w^T\tilde{x} + b$ can be expressed as follows:

$$S\left(\tilde{x}\right) = w^T\tilde{x} + b > 0 \ \text{ if } \tilde{x} \text{ is an instance of } C_1.$$

$$S\left(\tilde{x}\right) = w^T \tilde{x} + b < 0 \text{ if } \tilde{x} \text{ is an instance of } C_2.$$

The training phase of an SVM involves adjusting the weights and bias in order to achieve the separation of all instances belonging to classes C_1 and C_2 by the hyperplane. In regards to the hyperplane, the most favorable scenario is for it to be positioned as far as possible from the closest instances of both classes (Kim, 2017). It shoud be noted that any supervised classification model, including SVMs, requires a predefined set of input data, which involves the selection and collection of appropiate parameters. Additionally, the data needs to be labeled or categorized into classes (seismic, non-seismic), in order to train the model and make predictions for new inputs.

The implementation of an SVM classification model to distinguish between periods of seismic and non-seismic activity was performed using a programming and numeric computing platform specialized in data analysis, algorithm development, and model creation. As part of the SVM model implementation, the collected data was divided into two final datasets:

(1) The training set, which comprised 90% of the data, encompassed dates ranging from April 22, 2019, to December 06, 2015.
(2) The testing and final evaluation set constituted the remaining 10% of the data and covered dates between July 18, 2016, and September 2017.

In addition, since features constitute the most important part of classification problems, a set of 90 features was prepared considering the first eight days of each period (Table 4). These features were constructed using statistical data, results obtained from implemented analyses (such as kurtosis and skewness), and the evaluations conducted (detailed in Table 4). Moreover, to reduce the dimensions of the feature vector, Principal Component Analysis (PCA) was applied. The reduced features were then used as inputs for a Medium Gaussian SVM, using a Gaussian kernel function with a kernel scale of 1.4. The SVM model was trained using a box constraint level of 1 and the one-vs-one multiclass method.

3. Results and discussions

The main difference observed between seismic and non-seismic periods in this study was the magnitude of VTEC. Generally, seismic events reached up to 40 TEC units (TECU), while the non-seismic periods remained below 30 TECU (Fig. 11). Furthermore, the VTEC during seismic periods presented higher maximum and average values compared to the overall period under study (Fig. 4 and Fig. 10). However, the higher VTEC values recorded during seismic events do not necessarily indicate a precursor phenomenon. The ionosphere, being a medium easily influenced by external factors such as Space Weather, can contribute to the observed variations. Additionally, the effects of ionosphere perturbations caused by physical mechanisms can not be denied.

These mechanisms include direct acoustic waves generated by vertical crustal movements (Heki et al. 2006), ionospheric effects induced by aerosols and metallic ions propagated in the atmosphere (Pulinets et al. 1994), and the alpha decay of gas radon emitted from the Earth's crust (Heki, 2011), among others. It should be noted that even factors unrelated to seismic activity can influence the state of the ionosphere (Zaslavski et al., 1998).

In order to analyze variations related to season and geographic location, the periods were divided based on month, year, and data collection site. In Fig. 5, three events from the year 2015 are shown. It can be observed that seismic periods exhibit higher variations in VTEC, as indicated by the larger standard deviations. Also, the mean VTEC values range between 20 and 40 UTEC. In contrast, the

Table 4
The selected features for the SVM classification model.

Number	Feature
1	Daily mean of VTEC.
2	Daily standard deviation of VTEC.
3	Daily variance of VTEC.
4	Daily maximum value of VTEC.
5	Daily minimum value of VTEC.
6	Evaluation of daily geomagnetic D*st* index. If < -50 nT, then assigned 1, otherwise assigned 0.
7	Evaluation of daily solar F10.7 index. If > 120 s.f.u., then assigned 1, otherwise assigned 0.
8	Daily number of sunspots (R).
9	Daily Mean-Squared Error (MSE) of VTEC.
10	Evaluation of daily solar flares (M1 - X7 classes) releases. If true, then assigned 1. If false, assigned 0.
11	Daily maximum value of solar F10.7 index.
12	Daily minimum value of solar F10.7 index.
13	Maximum value of geomagnetic Kp index.
14	Daily variations in the VTEC mean.
15	Season of the year per period.
16	Value for skewness based on cross-correlation results.
17	Value for kurtosis based on cross-correlations results.

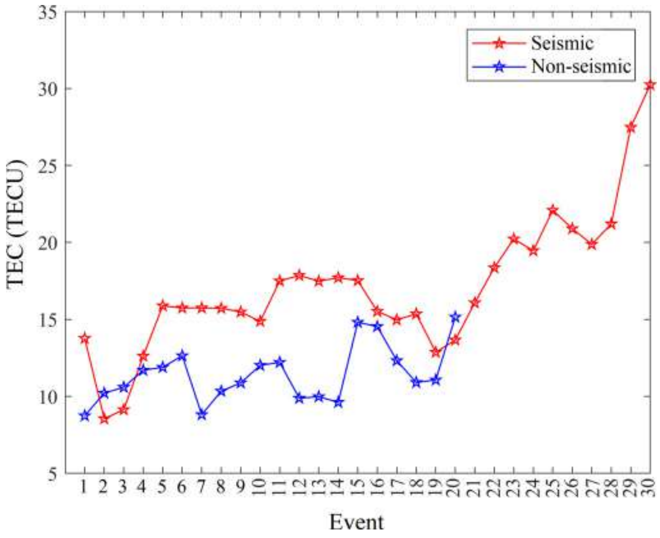

Fig. 4. The average VTEC for the complete seismic and non-seismic periods.

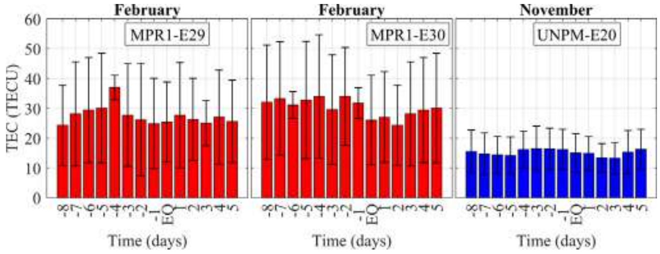

Fig. 5. Mean and standard deviation of VTEC per day for events in 2015, with events identified as “E” followed by its number. Data collection site denoted to the left of event number. Seismic events shown with red bars, non-seismic periods with blue bars. X-axis indicates days before and after the earthquake (“EQ”).

non-seismic periods generally remain below 20 TECU. Fig. 6 further highlights the significantly difference in standard deviation between earthquake-related events and non-seismic periods.

Fig. 7 illustrates the mean VTEC and standard deviation for the non-seismic periods of January and December 2017. Despite being located in different regions, these periods exhibit a low variation in both mean VTEC and standard deviation. Furthermore, the mean VTEC and standard deviation for events recorded in September 2017 from Oaxaca and Chiapas display similarities.

In Fig. 8, the mean VTEC of seismic event 3 is shown, which is the only recorded event in Baja California Sur, located in the Northwest region of Mexico. The mean VTEC during this event was slightly above 10 TECU. The corresponding standard deviation indicates that there were minor variations in the VTEC values throughout this seismic event. However, the non-seismic periods recorded in the Eastern state of Quintana Roo during the same year exhibited similar mean VTEC values and a low standard deviation, particularly in the month of February.

For Figs. 5–9 the mean VTEC was calculated using the complete period of days corresponding to each event. In general, most of the non-seismic events showed lower mean VTEC values compared to the earthquake events. However, the VTEC values for the seismic events 2 and 3 were even lower than the mean VTEC values of the non-seismic events (Fig. 10). In fact, these two seismic events had the lowest mean VTEC values and were recorded in January of 2019 and 2018, respectively. On the other hand, the seismic events occurring between 2015 and 2016 registered the highest mean VTEC values.

Moreover, from Figs. 5–9, some questions were formulated regarding the changes in mean VTEC before, during, and after the earthquakes studied, as well as how this change compares with non-seismic periods. First, how does the mean VTEC change before, during, and after earthquakes? The mean number of days with VTEC increments was 3.5 days, with most events showing VTEC increments within 3 to 4 days before the earthquakes. The maximum increment observed was 6.92 TECU, and the maximum decrement was 9.23 TECU. The minimum increment and decrement were 0.39 and 0.48 TECU, respectively.

During the days of the main shock, increments and decrements remained equal. The maximum increment was 2.83 TECU (Event 24) and the maximum decrement was 5.69 TECU (Event 30). After the earthquake, VTEC decrements predominated, with 21 of 30 events showing more days with decrements. The maximum increment during this period was 5.53 TECU (Event 4), and the maximum decrement was 9.25 TECU (Event 26).

This raised the final question, does the mean VTEC tend to decrement after an earthquake? After the earthquakes studied, the mean VTEC tends to decrement. The mean number of days with VTEC increments was 2.13, occurring within 1 to 2 days after the main shock. On the other hand, VTEC decrements had an average of 2.86 days, occurring within 2 to 3 days after the main shock.

The absolute values (| |) of the maximum increment and decrement of the mean VTEC for the periods before, during and after the earthquake were as follows: |6.92 TECU| and |9.23 TECU|, |2.83 TECU| and |5.69 TECU|, |5.53 TECU| and |9.25 TECU|, respectively. This indicates a high variability, with the maximum decrements in the mean VTEC showing greater values.

In comparison with the non-seismic periods, most events (15 out of 20) presented days with VTEC decrements, and only 5 events showed increments in most of the days. The maximum increment and decrement observed was 3.47 TECU and 4.43 TECU, respectively. The absolute values (| |) for non-seismic periods were: |3.32 TECU| and |2.83 TECU|, |1.21 TECU| and |1.20 TECU|, |3.47 TECU| and |4.43 TECU| for increments and decrements, respectively. In this case, the variability of VTEC was smaller, and a different trend was observed compared to seismic events.

The consecutive geomagnetic storms depicted in Fig. 11 correspond to the seismic events 11,12,13,14 and 15, which occurred from September 8 to 12, 2017. In this particular

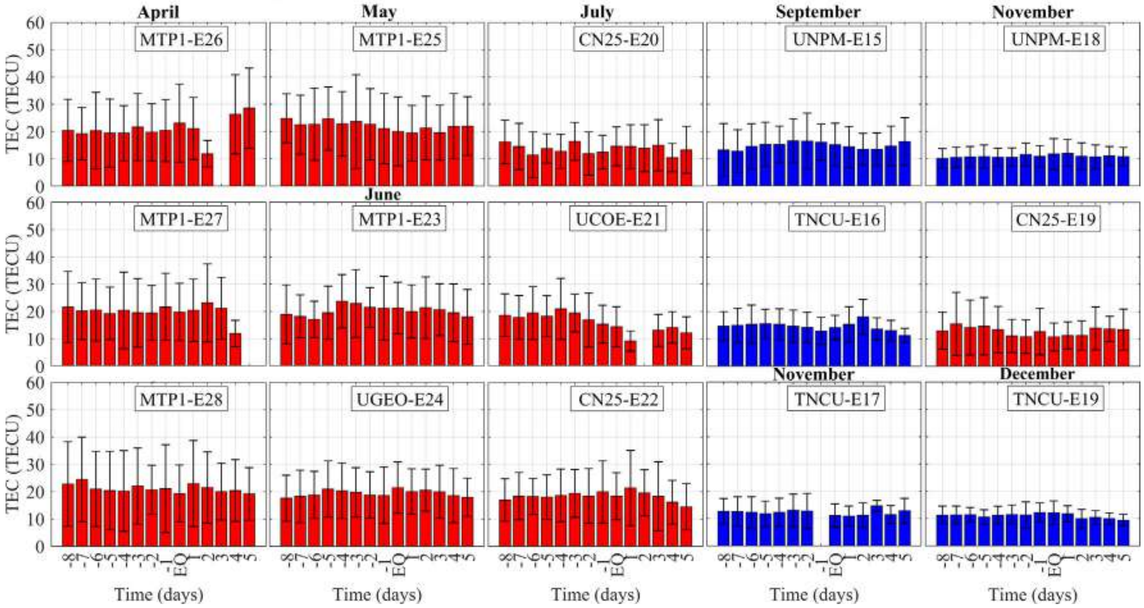

Fig. 6. Mean and standard deviation of VTEC per day for events in 2016, with events identified as "E" followed by its number. Data collection site denoted to the left of event number. Seismic events shown with red bars, non-seismic periods with blue bars. X-axis indicates days before and after the earthquake ("EQ").

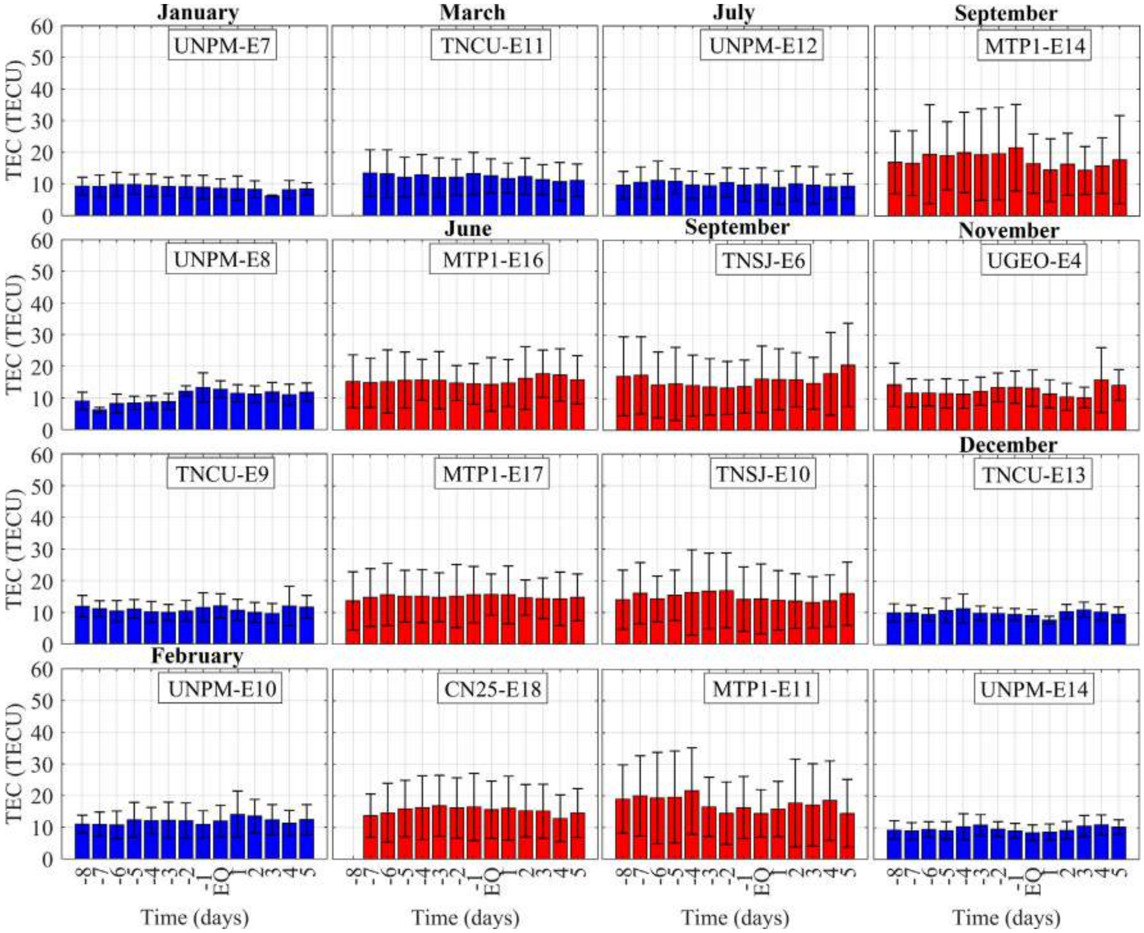

Fig. 7. Mean and standard deviation of VTEC per day for events in 2017, with events identified as "E" followed by its number. Data collection site denoted to the left of event number. Seismic events shown with red bars, non-seismic periods with blue bars. X-axis indicates days before and after the earthquake ("EQ").

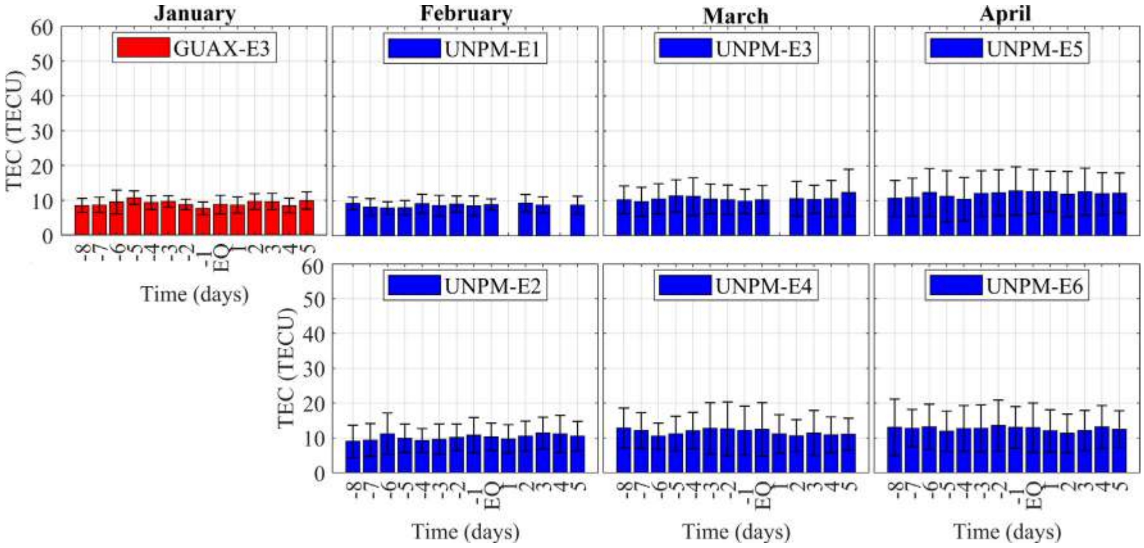

Fig. 8. Mean and standard deviation of VTEC per day for events in 2018, with events identified as "E" followed by its number. Data collection site denoted to the left of event number. Seismic events shown with red bars, non-seismic periods with blue bars. X-axis indicates days before and after the earthquake ("EQ").

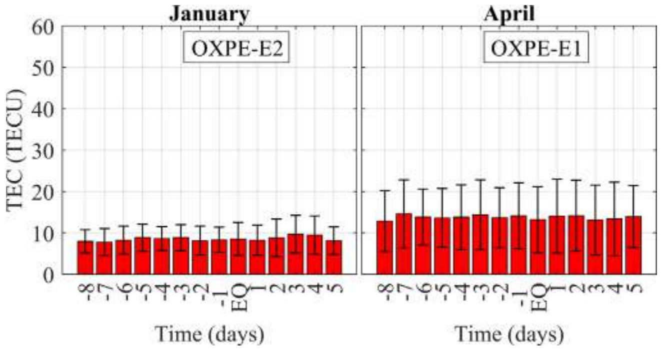

Fig. 9. Mean and standard deviation of VTEC per day for seismic events in 2019, with events identified as "E" followed by its number. Data collection site denoted to the left of event number. X-axis indicates days before and after the earthquake ("EQ").

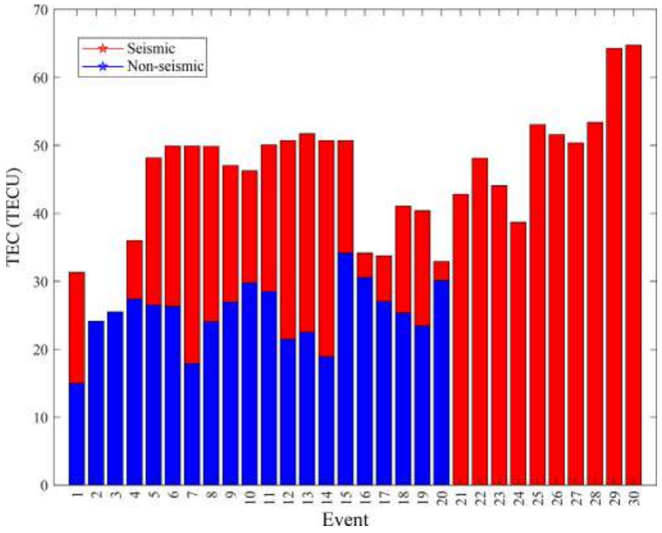

Fig. 10. Maximum VTEC values recorded in the period of days considered per event.

case, these intense solar-terrestrial disturbances were associated with Space Weather phenomena that occurred during the month of September 2017.

The reference value for non-quiet conditions of Dst < -20 nT was selected based on the values used in Akhoondzadeh et al. (2010). Therefore, most of both the seismic and non-seismic periods in this study exhibited disturbed geomagnetic conditions (Fig. 12). However, the VTEC during seismic events was higher, particularly in events 1 and 2. In general, 19 non-seismic periods exceeded the Dst threshold of $<$ -20 nT (95% of the dataset), while 28 seismic events (93.33% of the dataset) also surpassed this threshold (Fig. 12).

Additionally, a vertical black dotted line was placed at 30 TECU in Fig. 12 to assess the VTEC values. This considering the maximum VTEC value recorded in the non-seismic periods, which was 34.13 TECU (Event 15). The analysis reveals that 24 seismic events (80% of the dataset) surpassed the maximum VTEC value recorded in the non-seismic periods. This indicates a higher VTEC magnitude during seismic events compared to non-seismic periods.

The solar and geomagnetic indices have been used as a valuable tool to distinguish between ionospheric disturbances associated with solar activity and those possibly related to earthquakes. In this sense, the following solar and geomagnetic indices were analyzed: the F10.7 index, R, SSN (Sunspot Number), Kp index and Dst index. Also, to evaluate the behavior of these indices, specific reference values were selected. Kp index values exceeding 3 units were considered indicative of disturbed conditions (Thomas et al., 2017). Additionally, disturbed conditions

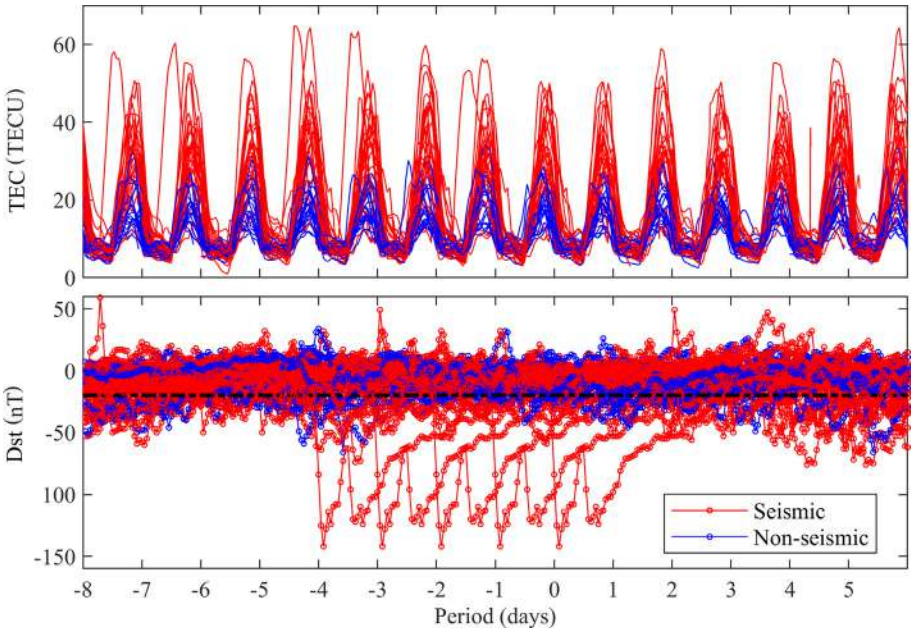

Fig. 11. VTEC and Dst index for the events under study.

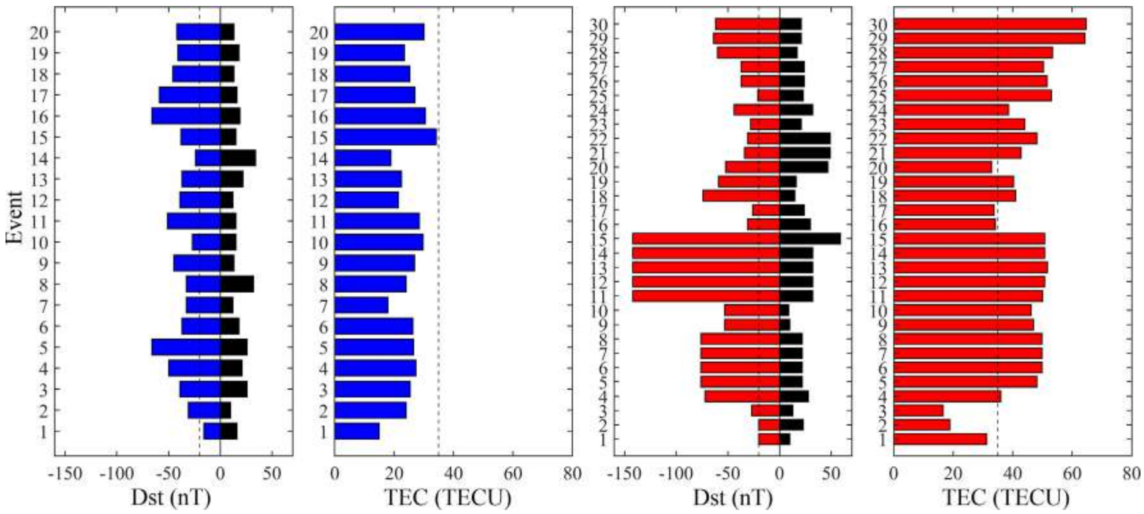

Fig. 12. Maximum values obtained per event for the Dst index and VTEC. The vertical black dotted lines indicate the reference values of −20 nT and 30 TECU. On the right side, seismic events are shown in red color, and on the left side, non-seismic periods are displayed in blue color.

were associated with F10.7 index values > 120 solar flux units (s.f.u.) (Kim et al., 2017).

In Fig. 13, the colored sections represent the disturbed days for each event, based on the previously defined reference values (Kp > 3, Dst < -20 nT, F10.7 > 120 s.f.u.). Notably, the solar index F10.7 exhibited the fewest disturbed days during both earthquake and non-seismic periods. However, these disturbed days were concentrated between September 8 to September 12, 2017, which corresponds to the time period of seismic events 11 to 15 (Fig. 11).

During this particular period, the intense solar-terrestrial disturbances were likely caused by the solar active region named “AR2673”, which produced multiple X-class solar flares from September 4 to September 10, 2017. This activity included a strong solar flare (X9.3) recorded on September 6, 2017 (Fig. 2). Following this flare, a severe geomagnetic storm (type G4) occurred on September 7 and 8, 2017, and a second strong solar flare (X8.2) on September 10, 2017, during solar cycle 24.

It should be noted that after the main flare (X9.3), a strong earthquake (M_w = 8.2, Event 15 of Table 1) occurred on September 8, 2017, at 04:49 UT, with the epicenter located off the Pacific coast of Oaxaca. This earthquake was the strongest recorded in Mexico since 1932. Furthermore, 11 days after, on September 19 (18:14 UT) another earthquake (M_w = 7.1) took place at the border of Puebla and Morelos in Mexico (Dorman et al., 2019).

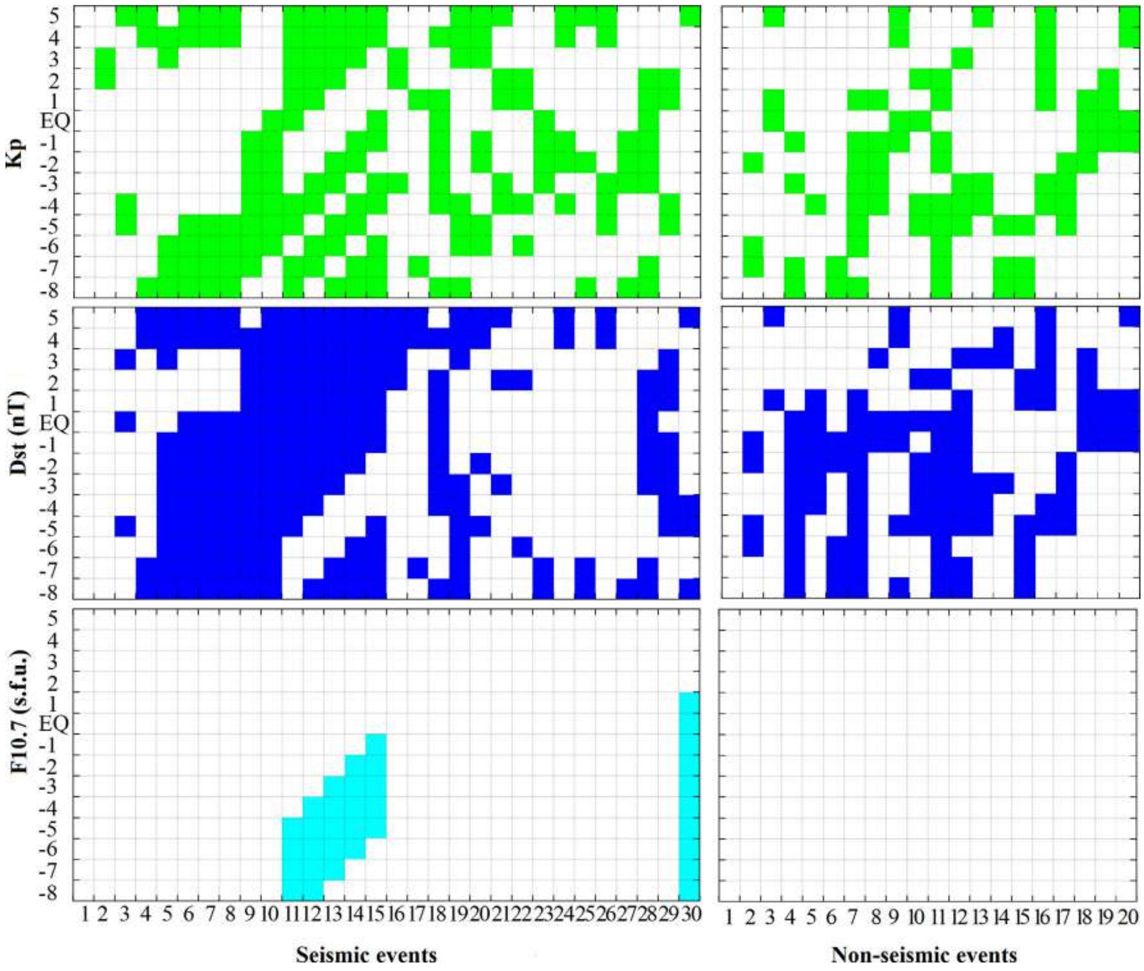

Fig. 13. The y-axis represents the time in days, with the reference point being the earthquake day ("EQ"). The colored sections in each panel indicate the days that surpassed the defined threshold for evaluating the Kp, Dst and F10.7 indices.

Furthermore, Fig. 13 illustrates that seismic events 5 to 15, totaling 11 events, exhibited the highest accumulation of disturbed days based on the Dst index, using the previously defined threshold (i.e., Dst < -20 nT). During these events, at least 78% (11 days) of the study period experienced disturbances. Also, these seismic events occurred in 2017, which recorded the highest number of seismic events ($M_w \geq 5$) considered in this study (15 out of 30).

The analysis of disturbed days during the period corresponding to seismic events revealed that the Dst index was the most recurrent (46%), followed by the Kp index with 38%, while the F10.7 index showed the least likelihood of surpassing the defined threshold (8%) (Fig. 13). Likewise, the disturbed days during non-seismic periods exhibited similar patterns. In specific, the occurrences of disturbed days for non-seismic periods were as follows: Dst index (38%) and Kp index (28%). However, disturbances in the F10.7 index did not occur during any non-seismic period in this study. In general, the days that exceeded the defined threshold for the evaluation of the Dst index were 8.4% more recurrent during seismic events than during non-seismic periods (46% vs 38%, respectively).

The results from the cross-correlation analysis were also analyzed for both seismic and non-seismic periods. Some of the selected characteristics used to evaluate the cross-correlation contribute to the classification objectives. For example, the type of skew distribution between classes allows for classification based on biases. Additionally, the different skewness of the distributions within the classes helps explain the data characteristics. Therefore, skewness is a useful measure to achieve the classification objectives (Suthaharan, 2016).

The fit, kurtosis and inclination were also analyzed. To calculate the level of bias from the cross-correlation analysis, the following conditions were considered: if the value was less than -1 or > 1, the data was considered highly skewed. If the value fell between -1 and -0.5 or between 0.5 and 1, then the data was moderately biased. Regarding inclination, a value greater than zero indicated a positive skew to the right. To determine the adjustment, the length of the signal was considered. For example, if the highest point of the distribution equaled the signal length, the fit was considered at zero.

For asymmetry, a value greater than – 0.5 and less than 0.5 denoted an approximately symmetric distribution. If the value was equal to zero, the distribution was considered perfectly symmetric; otherwise, it was asymmetric. Moreover, to determine the type of kurtosis and its excess, the following conditions were established: a value equal to 3 indicated a Mesokurtic type, a value less than 3 denoted a Platykurtic type, and a kurtosis value > 3 corresponded to a Leptokurtic type.

In general, the previous analyses and results formed part of the selection and collection process of competent parameters considered for the machine learning technique. The features selected for machine learning are listed in Table 4. Furthermore, to assess the results from the SVM model, the confusion matrix for the training set is shown in Fig. 14. The accuracy scores were compute using k-fold cross-validation (k = 5), and the average cross-validation error is reported. The SVM model indicated a validation accuracy of 88.9% for the training set. Specifically, the following training result metrics were obtained: Accuracy (Validation): 88.9%, Total misclassification cost (Validation): 5, Prediction speed: ~600 obs/sec, Training time: ~0.79 sec.

Positive Predictive Values, or PPV in the confusion matrices, refers to the percentage of successfully classified observations per predicted class. Further, the percentage of incorrectly classified observations per predicted class is known as FDR, or False Discovery Rates. After training the model, the performance of the test set was evaluate. The following test set metrics were compute: Accuracy (Test): 80%, Total cost (Test): 1. The confusion matrix for the test set is shown in Fig. 15.

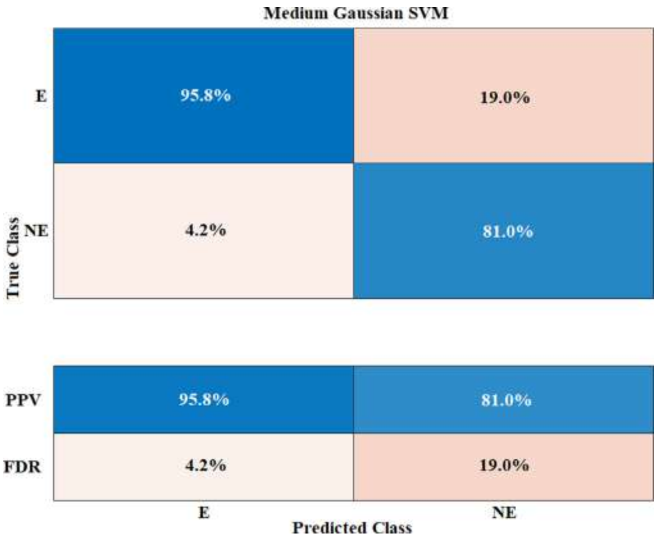

Fig. 14. Confusion matrix results for the training set per predicted class. Positive predictive values (correctly predicted points) are displayed in blue for each class. Conversely, false discovery rates (incorrectly predicted points) are indicated in peach color for each class. Class E stands for earthquake-related events and NE for non-seismic periods.

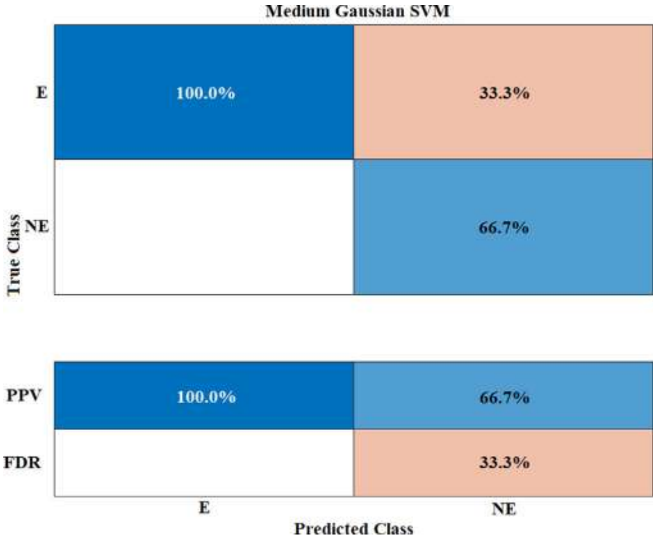

Fig. 15. Confusion matrix results for the test set per predicted class. Positive predictive values (correctly predicted points) are displayed in blue for each class. Conversely, false discovery rates (incorrectly predicted points) are indicated in peach color for each class. Class E stands for earthquake-related events and NE for non-seismic periods.

Among the limitations of the current study, the sample size stands out. While a larger sample size typically enhances the reliability and accuracy of a machine learning model, the initial approach adopted in this study for classifying seismic events from non-seismic periods demonstrated promising results, considering the specified parameters and the days included in the proposed study. Undoubtedly, these techniques present an interesting opportunity for real-time monitoring. However, the study acknowledges that data collection plays a crucial role in the application of such approaches. This includes the selection of non-seismic periods and the number of seismic events considered within the study area.

Moreover, it is essential to choose a model assessment technique that better fits the sample size, the physical aspects of the data, and the computational cost. Addressing these limitations in future studies will be critical to advancing the field. Furthermore, it should be noted that statistical analysis and evaluation of various study cases are essential for the development of earthquake precursor studies (Akhoondzadeh, 2019). These considerations will help refine and improve the accuracy of earthquake prediction models.

4. Conclusions

The development of society points to a future in which the collection, analysis and use of data will increase, and computer methods such as machine learning will benefit from this. Hence, as technology develops and more data is being analyzed, the opportunity to delve deep into the field of earthquake forecasting arises. In this study, VTEC along with different geomagnetic and solar indices were obtained with the aim of applying an initial approach of a machine learning model capable of classifying between periods of seismic and non-seismic activity.

The analysis was performed considering a 14 day period. A set of 30 seismic and 20 non-seismic periods was considered. The ground motions were registered in Mexico. According to the results, seismic events presented higher VTEC values than the non-seismic periods. This difference was significant for most of the events. Regarding the period of years under study, the non-seismic periods occurred between 2015 and 2018, while the seismic events occurred between 2015 and 2019. Therefore, possible temporal variations were likely negligible.

Moreover, 46% of the total days with seismic events presented values that exceeded the quiet threshold defined for the Dst index (<- 20 nT), compared to 38% of the non-seismic periods. Among the considered solar and geomagnetic indices the least recurrent for seismic and non-seismic periods was the F10.7 solar index (8% vs 0%, respectively). Furthermore, considering the studied events, it was more likely that a seismic event occurred in a month where a solar flare of M1-X7 type was registered (66% for seismic events vs 20% for non-seismic events).

On the other hand, the use of machine learning facilitated the handling and application of a considerable amount of different types of data. However, it is important to take into account the physical characteristics of the data during analysis. Additionally, it allowed to demonstrate that Support Vector Machines (SVM) represents a good opportunity for this approach. In this manner, the results from the SVM model indicated a validation accuracy of 88.9% for the training set, and an accuracy of 80% was achieved for the test set. Finally, the existence of a potential relation between earthquakes and the parameters under study was not evident. Nevertheless, to explore this further, it would be necessary to consider alternative analyses and methods.

Declaration of Competing Interest

The authors declare that they have no known competing financial interests or personal relationships that could have appeared to influence the work reported in this paper.

Acknowledgements

The authors would like to express their gratitude to UNAVCO and CORS networks for making the GPS measurement data freely available. We would also like to extend our sincere gratitude to the Global Data Center SILSO in Brussels, the Space Weather Program of Canada, the World Data Centers in Russia, the NASA OMNIWeb data explorer, and the National Seismological Service in Mexico for sharing the data that underpinned this research.

Furthermore, we are thankful to the National Council of Humanities, Sciences, and Technologies (CONAHCyT) in Mexico for granting a scholarship that supported the completion of this study. Lastly, the authors wish to express their gratitude to the reviewers and editor for their valuable comments and insightful suggestions.

Appendix A. Supplementary data

Supplementary data to this article can be found online at https://doi.org/10.1016/j.asr.2023.08.028.

References

Akhoondzadeh, M., De Santis, A., 2022. Is the apparent correlation between solar-geomagnetic activity and occurrence of powerful earthquakes a casual artifact? Atmos. 13 (7), 1131. https://doi.org/10.3390/atmos13071131.

Akhoondzadeh, M., Parrot, M., Saradjian, M.R., 2010. Electron and ion density variations before strong earthquakes (M>6.0) using DEMETER and GPS data. Nat. Hazards Earth Syst. Sci. 10 (1), 7–18 https://doi:10.5194/nhess-10-7-2010.

Akhoondzadeh, M., 2019. Kalman filter and Neural Network methods for detecting irregular variations of TEC around the time of powerful Mexico (Mw=8.2) earthquake of September 08, 2017. Journal of the Earth and Space Physics. 44 (4), 87-97. https://doi:10.22059/jesphys.2018.258251.1007007.

Arikan, F., Shukurov, S., Tuna, H., et al., 2016. Performance of GPS slant total electron content and IRI-Plas-STEC for days with ionospheric disturbance. Geod. Geodyn. 7 (1), 1–10. https://doi.org/10.1016/j.geog.2015.12.009.

Astafyeva, E., Heki, K., 2011. Vertical TEC over seismically active region during low solar activity. J. Atmos. Sol. Terr. Phys. 73 (13), 1643–1652. https://doi.org/10.1016/j.jastp.2011.02.020.

Barkat, A., Ali, A., Rehman, K., et al., 2018. Multi-precursory Analysis of Phalla Earthquake (July 2015; Mw 5.1) Near Islamabad. Pakistan. Pure Appl. Geophys. 175, 4289–4304. https://doi.org/10.1007/s00024-018-1927-5.

Bolt, B.A., 1993. Earthquakes and geological discovery. Scientific American Library, New York.

Bolt, B.A., 2001. The nature of earthquake ground motion. In: Naeim, F. (Ed.), The Seismic Design Handbook. Springer, Boston, MA. https://doi.org/10.1007/978-1-4615-1693-4_1.

Courboulex, F., Singh, S.K., Pacheco, J.F., et al., 1997. The 1995 Colima-Jalisco, Mexico, earthquake (Mw 8): A study of the rupture process. Geophys. Res. Lett. 24 (9), 1019–1022. https://doi.org/10.1029/97GL00945.

Delorey, A.A., Van Der Elst, N.J., Johnson, P.A., 2017. Tidal triggering of earthquakes suggests poroelastic behavior on the San Andreas Fault. Earth Planet. Sci. Lett. 460, 164–170. https://doi.org/10.1016/j.epsl.2016.12.014.

Deviren, N. M., Gulyaeva, T., Sezen, U., et al., 2014. Detection of Seismic Precursors Using Distance Metrics Between GPS-TEC and IRI-Plas, 40th COSPAR Scientific Assembly.

Dorman, L., Tassev, Y., Velinov, P., et al., 2019. Investigation of exceptional solar activity in September 2017: GLE 72 and unusual Forbush decrease in GCR. J. Phys.Conference Series. 1181. https://doi.org/10.1088/1742-6596/1181/1/012070 012070.

Godinez-Dominguez, E., Tena-Colunga, A., Perez-Rocha, L.E., et al., 2021. The September 7, 2017 Tehuantepec, Mexico, earthquake: Damage assessment in masonry structures for housing. Int. J. Disaster Risk Reduct. 56. https://doi.org/10.1016/j.ijdrr.2021.102123.

Gousheva , M. N., Georgieva, K. Y., Kirov, B. B., et al., 2003. On the relation between solar activity and seismicity. International Conference on Recent Advances in Space Technologies. RAST '03. Proceedings of Istanbul, Turkey, 236-240. 10.1109/RAST.2003.1303913.

Han, Y., Guo, Z., Wu, J., et al., 2004. Possible triggering of solar activity to big earthquakes (Ms $\geq$ 8) in faults with near west-east strike in

China. Sci. China Ser. G.: Phy. & Ast. 47, 173–181. https://doi.org/10.1360/03yw0103.

Heki, K., 2011. Ionospheric electron enhancement preceding the 2011 Tohokuoki earthquake. Geophys. Res. Lett. 38 (17). https://doi.org/10.1029/2011GL047908.

Heki, K., Otsuka, Y., Choosakul, N., et al., 2006. Detection of ruptures of Andaman fault segments in the 2004 Great Sumatra Earthquake with coseismic ionospheric disturbances. J. Geophys. Res. 111, B09313. https://doi.org/10.1029/2005JB004202.

Jiang, C., Wei, X., Cui, X., et al., 2009. Application of support vector machine to synthetic earthquake prediction. Earthq. Sci. 22 (3), 315–320. https://doi.org/10.1007/s11589-009-0315-8.

Jin, X.X., 1996. Theory of carrier adjusted DGPS positioning approach and some experimental results. Delft University of Technology, Dissertation,.

Karatay, S., Arikan, F., Arikan, O., 2010. Investigation of total electron content variability due to seismic and geomagnetic disturbances in the ionosphere. Radio Sci. 45 (5), RS5012. https://doi.org/10.1029/2009RS004313.

Kim, V., Hegai, V.V., Liu, J.Y., et al., 2017. Time-varying seismogenic coulomb electric fields as a probable source for pre-earthquake variation in the ionospheric F2-Layer. Journal of Astronomy and Space Sciences. 34 (4), 251–256. https://doi.org/10.5140/JASS.2017.34.4.251.

Kim, P., 2017. Matlab Deep Learning: With machine learning, neural networks and artificial intelligence, 1st ed., USA: Apress, Berkeley, CA. 10.1007/978-1-4842-2845-6.

Le, H., Liu, J.Y., Liu, L., 2011. A statistical analysis of ionospheric anomalies before 736 M6.0+ earthquakes during 2002–2010. J. Geophys. Res. 116 (A2). https://doi.org/10.1029/2010JA015781.

Love, J.J., Thomas, J.N., 2013. Insignificant solar-terrestrial triggering of earthquakes. Geophys. Res. Lett. 40, 1165–1170. https://doi.org/10.1002/grl.50211.

Marchitelli, V., Harabaglia, P., Troise, C., et al., 2020. On the correlation between solar activity and large earthquakes worldwide. Sci. Rep. 10, 11495. https://doi.org/10.1038/s41598-020-67860-3.

Marques, H.A., Monico, J.F.G., Aquino, M., 2011. RINEX_HO: second and third-order ionospheric corrections for RINEX observations files. GPS Solut. 15, 305–314. https://doi.org/10.1007/s10291-011-0220-1.

Mayaud, P.N., 1980. Derivation, meaning and use of geomagnetic indices. American Geophysical Union, Washington. https://doi.org/10.1029/GM022.

Melgarejo-Morales, A., Vazquez-Becerra, G.E., Millan-Almaraz, J.R., et al., 2020. Examination of seismo-ionospheric anomalies before earthquakes of Mw $\geq$ 5.1 for the period 2008–2015 in Oaxaca. Mexico using GPS-TEC. Acta Geophys. 68, 1229–1244. https://doi.org/10.1007/s11600-020-00470-9.

Muhammad, A., Külahcı, F., Birel, S., 2023. Investigating radon and TEC anomalies relative to earthquakes via AI models. J. Atmos. Sol. Terr. Phys. 245. https://doi.org/10.1016/j.jastp.2023.106037.

Odintsov, S., Boyarchuk, K., Georgieva, K., et al., 2006. Long-period trends in global seismic and geomagnetic activity and their relation to solar activity. Phys. Chem. Earth, Parts A/B/C. 31, 88–93. https://doi.org/10.1016/j.pce.2005.03.004.

Ouzounov, D., Pulinets, S., Romanov, A., et al., 2011. Atmosphere-ionosphere response to the M9 Tohoku earthquake revealed by multi-instrument space-borne and ground observations: Preliminary results. Earthq. Sci. 24, 557–564. https://doi.org/10.1007/s11589-011-0817-z.

Pulinets, S. A., Legen'ka, A. D., & Alekseev, V. A., 1994. Pre-earthquake ionospheric effects and their possible mechanisms in dusty and dirty plasmas, noise, and chaos in space and in the laboratory. Springer, New York. 10.1007/978-1-4615-1829-7_46.

Sardon, E., Rius, A., Zarraoa, N., 1993. Estimación del contenido total de electrones en la ionosfera usando datos del sistema de posicionamiento global. Física de la Tierra. 5, 167–182.

Shah, M., Tariq, M.A., Naqvi, N.A., 2019. Atmospheric anomalies associated with Mw > 6.0 earthquakes in Pakistan and Iran during 2010–2017. J. Atmos. Sol. Terr. Phys. 191. https://doi.org/10.1016/j.jastp.2019.06.003.

Shah, M., Calabia, A., Tariq, M.A., et al., 2020. Possible ionosphere and atmosphere precursory analysis related to Mw > 6.0 earthquakes in Japan. Remote Sens. Environ. 239. https://doi.org/10.1016/j.rse.2019.111620.

Shah, M., Abbas, A., Ehsan, M., et al., 2021. Ionospheric-Thermospheric responses in South America to the August 2018 geomagnetic storm based on multiple observations. IEEE J. Sel. Top. Appl. Earth Obs. Remote Sens. 15, 261–269. https://doi.org/10.1109/JSTARS.2021.3134495 7.

Shah, M., Abbas, A., Adil, A., et al., 2022a. Possible seismo-ionospheric anomalies associated with Mw > 5.0 earthquakes during 2000–2020 from GNSS TEC. Adv. Space Res. 70 (1), 179–187. https://doi.org/10.1016/j.asr.2022.04.025.

Shah, M., Ehsan, M., Abbas, A., et al., 2022b. Possible thermal anomalies associated with global terrestrial earthquakes during 2000–2019 based on MODIS-LST. IEEE Geosci. Remote Sens. Lett. 19, 1–5. https://doi.org/10.1109/LGRS.2021.3084930.

Singh, O.P., Chauhan, V., Singh, V., et al., 2009. Anomalous variation in total electron content (TEC) associated with earthquakes in India during September 2006–November 2007. Physics and Chemistry of the Earth, Parts A/B/C. 34 (6–7), 479–484. https://doi.org/10.1016/j.pce.2008.07.012.

Singh, S.K., Ponce, L., Nishenko, S.P., 1985. The great Jalisco, Mexico, earthquakes of 1932: Subduction of the Rivera plate. Bull. Seismol. Soc. Am. 75 (5), 1301–1313. https://doi.org/10.1785/BSSA0750051301.

Sotomayor-Beltran, C., 2019. Ionospheric anomalies preceding the low-latitude earthquake that occurred on April 16, 2016 in Ecuador. J. Atmos. Sol. Terr. Phys. 182, 61–66. https://doi.org/10.1016/j.jastp.2018.11.003.

Suthaharan, S., 2016. Supervised Learning Algorithms. Machine Learning Models and Algorithms for Big Data Classification. Integrated Series in Information Systems, vol 36. Springer, Boston, MA. https://doi.org/10.1007/978-1-4899-7641-3_8.

Teunissen, P. J., 1991. The GPS phase-adjusted pseudorange. In: Proceedings of the second international workshop on high precision navigation, Stuttgart, 115–125.

Thomas, J.N., Huard, J., Masci, F., 2017. A statistical study of global ionospheric map total electron content changes prior to occurrences of M > 6.0 earthquakes during 2000–2014. J. Geophys. Res. Space Phys. 122 (2), 2151–2161. https://doi.org/10.1002/2016JA023652.

Tsai, Y. B., Liu, J. Y., Shin, T. C., et al., 2018. Multidisciplinary Earthquake Precursor Studies in Taiwan. In: Ouzounov, D., Pulinets, S., Hattori, K. and Taylor, P. (Eds.), Pre-Earthquake Processes. Pp. 41- 65. 10.1002/9781119156949.ch4.

Tsugawa, T., Saito, A., Otsuka, Y., et al., 2011. Ionospheric disturbances detected by GPS total electron content observation after the 2011 off the Pacific coast of Tohoku Earthquake. Earth Planets Space 63, 66. https://doi.org/10.5047/eps.2011.06.035.

Urata, N., Duma, G., Freund, F., 2018. Geomagnetic Kp Index and Earthquakes. Open Journal of Earthquake Research. 7 (1), 39–52. https://doi.org/10.4236/ojer.2018.71003.

Zaslavski, Y., Parrot, M., Blanc, E., 1998. Analysis of TEC measurements above active seismic regions. Phys. Earth Planet Int. 105, 219–228. https://doi.org/10.1016/S0031-9201(97)00093-9.